Synthesis and characterization of Er3+/Cu+-codoped fluorophosphate glasses

N. Abdedou, T. Djouama, M. Chalal, M. Poulain, B. Capoen, R. Mahiou

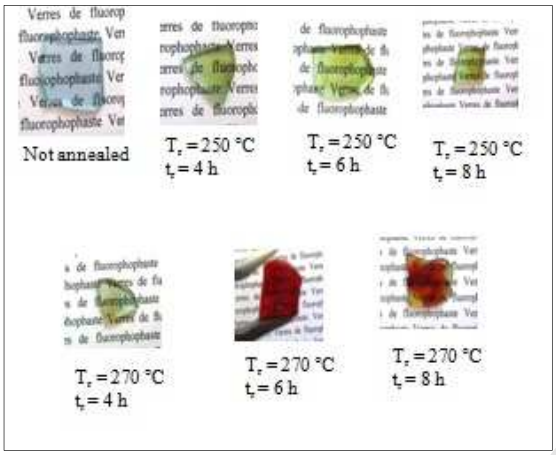

Synthesis and characterization of Er^{3+}/Cu^{+}-codoped fluorophosphate glasses

N. Abdedou[1], T. Djouama[1,*], M. Chalal[1, 2], M. Poulain[3], B. Capoen[4], R. Mahiou[5,*]

[1]Laboratoire d'Electronique Quantique, Faculté de Physique, USTHB, El-Alia, Bab-Ezzouar, 16111 Alger, Algérie

[2]Département de Physique, Faculté des Sciences, UMBB, 35000 Boumerdès, Algérie

[3]Institut des Sciences Chimiques de Rennes UMR CNRS 6226, Campus de Beaulieu, Université de Rennes1, 35042 Rennes, France

[4]Univ-lille, CNRS, UMR8523-PhLAM-Physique des Lasers Atomes et Molécules, CERLA/IRCICA, F-59000 Lille, France

[5]Université Clermont Auvergne, Institut de Chimie de Clermont Ferrand UMR 6296 CNRS/UBP/Sigma Clermont, Campus des Cézeaux, TSA 60026-CS 60026, F-63000 Clermont-Ferrand, France

[*]Corresponding Authors: torkia.djouama@gmail.com, rachid.mahiou@uca.fr

ABSTRACT

$NaPO_3$-ZnF_2 binary fluorophosphate glasses doped with trivalent erbium and monovalent copper were synthesized by the conventional melting and casting method using ErF_3 and CuCl as starting materials.The samples were systematically investigated using X-ray diffraction (XRD), energy dispersive X-ray spectroscopy (EDS), Fourier-transform infrared spectroscopy (FTIR), scanning electron microscopy (SEM) and transmission electron microscopy (TEM) analysis. X-ray powder diffraction patterns confirmed that the as-prepared compounds were all amorphous.The glass transition temperature (T_g) was observed around 230°C by DSC analysis, while the thermal stability range (ΔT) was estimated to be between 90 and 140 °C. The measured value of the refractive index (n) was measured as 1.502 at a wavelength of 632.8 nm. Thermal annealing of the samples was performed at different temperatures above T_g for various heat-treatment times. During these steps, monovalent copper and sodium ions were expected to be reduced, forming metallic nanoparticles. This transformation lead to coloration changes, depending on the annealing time and temperature, with respect to the transparency of the glasses. These spectroscopic changes are related to the plasmonic effects induced by the presence of both Cu and Na metallic nanoparticles, which promote red shift due to absorption. The VIS-NIR absorption spectra of the prepared glasses were

investigated in the frame work of standard Judd-Ofelt (J-O) theory, which was used to determine the J-O intensity parameters, radiative transition probabilities and branching ratios for Er^{3+} ions embedded in the glasses. The calculated intensity parameters ($\Omega_{2,4,6}$) were compared to those obtained for Er^{3+} in several other glasses.

Keywords: Nanoparticles, Fluorophosphate glasses, Optics, Absorption, Judd-Ofelt theory

1. Introduction

The choice of the host material is an important parameter when one deals with improving the optical properties of glasses notably when they are activated by rare earth or transitions metal ions. Independently on the most current crystals, the glasses are considered as efficient hosts due to their peculiar optical and also luminescence properties. Among the conventional glass host matrices, phosphate based fluoride glass is one of the best glass host material when compared with other hosts [1, 2].

Due to these reasons fluorophosphate glasses have been the subject of numerous studies, mainly for optical applications, UV transmission, and rare earth-based lasers. Their low nonlinear refractive index makes them suitable for very high power lasers [2-4]. These glasses offer a number of advantages, such as stability against devitrification, simple preparation, flexible composition and high rare earth solubility in addition of their low phonon energy and wider optical transmission window ranging from UV to mid-IR [5-7]. Moreover, in phosphate glasses, it is difficult to eliminate hydroxyl groups (OH^-), however, it can be possible to minimizes their contribution in fluorophosphate glasses without protection in ambient atmosphere [8]. Among various rare earth ions, Er^{3+} is one of the most investigated ions for light detection and ranging (LIDAR), solar panels, spectroscopy, and bio-imaging [9] and as dopant in tellurite glasses as effective radiation shields [10].

The presence of metal nanoparticles (NPs) in glasses, which modifies the spectroscopic properties of rare earth (RE) ions, is a field of interest, since the plasmonic effect can modify the radiative rate of the emitter centres. Various papers have reported the effect of silver or gold nanoparticles which are generated by chemical reduction during the thermal treatment. For example, these NPs notably enhance the up-conversion emitted fluorescence of Er^{3+} in zinc-tellurite glasses [11, 12]. However, to the best of our knowledge, copper has never been studied for this purpose. This paper presents the structural and optical properties of 60mol% $NaPO_3$ - 40mol% ZnF_2 binary glasses in which Er^{3+} and Cu^+ cations were incorporated. These cations were introduced into the batch as fluoride and chloride respectively. Among rare-earth ions, Er^{3+} is an efficient luminescence centre in visible and

infrared (IR) regions, with applications for various photonic devices such as fibre lasers or optical amplifiers in the IR range, and also compact visible lasers.

We report here the physical properties of some fluorophosphate glass samples, omitting fluorescence spectra and luminescence decays, which will be the subject of a forthcoming paper. The spectral transmissions of the annealed glasses are discussed assuming the formation of Cu and Na NPs.

2. Experimental

Glass samples were prepared in a system comprising 60mol%$NaPO_3$-37.5mol%ZnF_2-0.5mol%CuCl-2mol%ErF_3. Starting materials were $NaPO_3$ (Alfa Aesar, >96%), ZnF_2 (Alfa Aesar, 98%), ErF_3 (Alfa Aesar, 99.9%) and CuCl (Aldrich, 98%). Powders were introduced into a long platinum crucible in order to limit exchanges with the external atmosphere. The temperature was increased gradually until melting was complete, namely at around 700 °C. Some volatile species (e.g. POF_3, HF) escaped from the melt, generating a gaseous buffer at the melt surface. Once melted, the batch was maintained in the liquid state for 10 min for homogenization. It was then cast in brass moulds preheated at 210 °C. In this way the cooling rate was lower, avoiding thermal shock. An annealing stage was implemented for 2h at 210 °C to release internal stresses.

Finally, the glasses were cooled to room temperature, following the cooling inertia of the furnace. After cooling the samples were polished and heat-treated at between 250 and 270°C for 4, 6, and 8 hours in order to thermally reduce Cu^+ ions to Cu^0 and consequently to increase the probability of nucleating and favour the growth of copper NPs. Table 1 presents the characteristics of the obtained glasses with respect to annealing time and temperature.

Table 1: Composition, labels, heat treatments and visual aspect of the considered glasses

Composition	Sample	Annealing temperature (T_r)	Annealing time (t_r)	Image
60%NaPO3-37.5%ZnF2-0.5%CuCl-2%ErF3	NZCE0	Not annealed	0	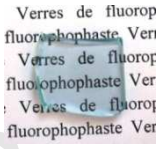
	NZCE5	250 °C	4 h	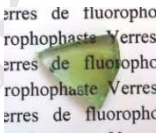
	NZCE6		6 h	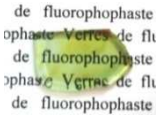
	NZCE7		8 h	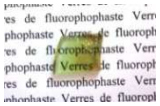
	NZCE9	270 °C	4 h	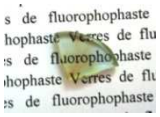
	NZCE10		6 h	
	NZCE11		8 h	

It can clearly be seen that the annealing treatment modifies the coloration of the obtained glasses. This colour modification is related to a shift of absorption bands, and possibly to the appearance of plasmonic effects under heat-treatment.

Fig. 1 shows the XRD pattern of the obtained NZCE0 glass as an example.

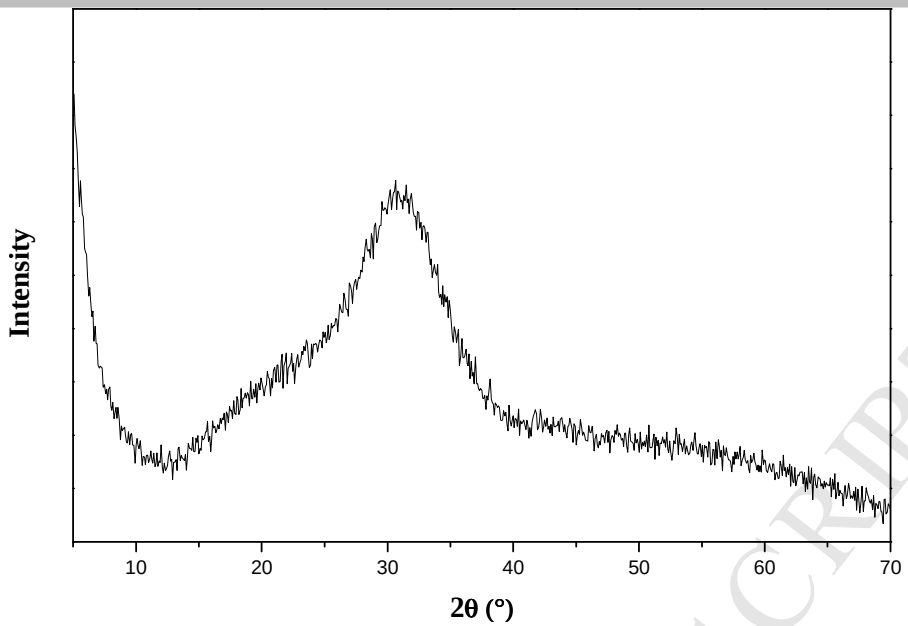

Fig. 1: XRD spectrum of the NZCE0 glass

The observed spectrum pattern clearly shows the amorphous character of the glass. Notably the $Zn_3(PO_4)_2$, which is the stable form of zinc phosphate crystal, is not observed, confirming the vitreous state of the samples. If copper or sodium NPs were assumed to exist inside this glassy matrix, the absence of a crystalline peak (especially at 2θ = 43.6° for the (111) reflection of metallic copper) is certainly due to the low concentration of these potential NPs arising from the reduction of Cu^+ and Na^+ ions to metal.

The thermal stability of a glass system with respect to crystallization can be defined as the temperature range $\Delta T = T_x - T_g$ (the difference between the onset of crystallization T_x and the glass transitiontemperatureT_g). Characteristic temperatures, namely T_g andT_x, were measured by DSC analysis (TA instruments DSC 2010) at a heating rate of 10 °C.min^{-1}, with a typical sample of 10 mg. The difference ΔT has frequently been quoted as a rough indicator of glass thermal stability against crystallization [3]. According to this criterion, a small ΔTmeans that, in the molten state beyond T_g, nucleation and crystal growth promote fast devitrification. The refractive index was measured using a metricon-type refractometer.

Infrared transmission spectra of the polished glass samples, having thicknesses around 2 mm, were recorded at room temperature using a BRUKER VECTOR22 spectrophotometer operating between 2500 and 8000cm^{-1}, and absorption spectra were obtained using a Perkin Elmer Precisely Lambda 1050 UV-VIS-NIR spectrophotometer operating between 200 and 2500 nm.

Transmission Electron Microscope (TEM) observations were performed using a FEI Tecnai G2 20 instrument operating at 200 kV, coupled with Energy-Dispersive X-ray Spectroscopy (EDS) measurements for chemical identification. Before analysis, carbon membrane-supported nickel

TEM grids were covered with powder grains from the finely-ground glass. A 3nm carbon film was then deposited onto the grid to achieve better electron conduction.

3. Results and discussion

3.1. Thermal properties and refractive index

The glass matrix chosen for this study was NZCE0, the DSC curve of which is shown in Fig. 2. The glass transition temperature was evaluated at 230°C ± 2°C and the thermal stability range ΔT ($T_x - T_g$) exceeded 130°C, which expresses good thermal stability before devitrification [5]. The refractive index (n) was 1.503 at 632.8 nm and 1.491 at 1550 nm. The results are presented in Fig.3. The experimental results (points in Fig.3) are fitted using Sellmeier's dispersion equation [13]:

$$n^2(\lambda) = 1 + \frac{S\lambda^2}{\lambda^2 - \lambda_0^2} \qquad (1)$$

The experimental values of the refractive index and Sellmeier's coefficients (S and λ_0) are shown in Table 2**.** Fig.3 shows that there is a good agreement between the experimental data and the fit.

Table 2: Experimental values and fitting values of the refractive index

Experimental points		Sellmeier's coefficients	
$\boldsymbol{\lambda}$ $(\boldsymbol{nm})$	**n**		
632.8	1.503 ± 0.002		
825.0	1.497 ± 0.002	**S**	1.196 ± 0.001
1311.0	1.492 ± 0.002	$\boldsymbol{\lambda_0}$ $(\boldsymbol{nm})$	117.563 ± 0.206
1551.0	1.491 ± 0.002		

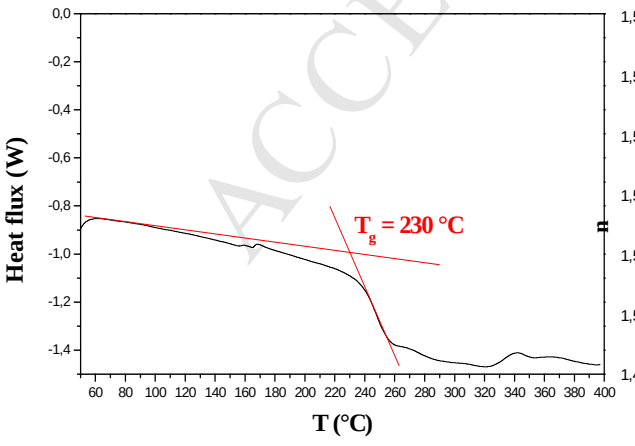

Fig. 2: DSC curve of NZCE0

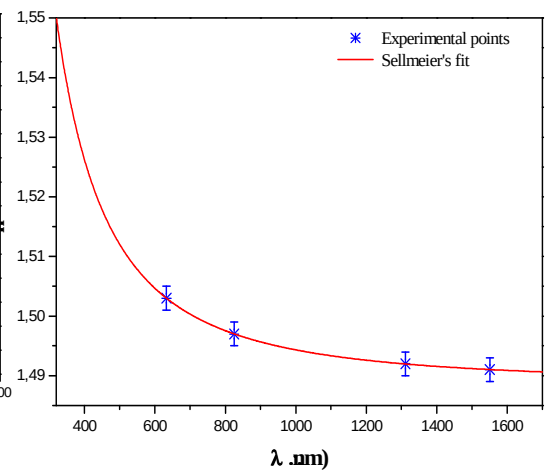

Fig. 3: Variation in the refractive index according to the wavelength fitted with Sellmeier's dispersion

3.2. UV-Visible-NIR spectroscopy

Fig.4 and Fig.5 illustrate the optical absorption spectra of glasses in the UV-Visible and near IR domains, for the two annealing temperatures of 250 °C and 270 °C respectively and for various annealing times. The absorption spectra exhibit thirteen Er^{3+} characteristic transitions from the ground state $^4I_{15/2}$ to the excited states $^2K_{15/2}$, $^4G_{9/2}$, $^4G_{11/2}$, $^2G_{9/2}$,$^4F_{3/2}$, $^4F_{5/2}$,$^4F_{7/2}$, $^2H_{11/2}$, $^4S_{3/2}$,$^4F_{9/2}$, $^4I_{9/2}$, $^4I_{11/2}$ and $^4I_{13/2}$. These narrow peaks are centred at about 356, 364, 378, 406, 441, 450, 486, 520, 542,650, 800, 970 and 1530 nm [14-16]. Table 3 shows the wavelengths corresponding to the different transitions, compared to those found in the literature.

Table 3**:** Wavelengths corresponding to the different absorption transitions of Er^{3+}

N°	Transition	Wavelength in this work (nm)	Literature wavelength with reference (nm)
01	$^4I_{15/2} \rightarrow ^2K_{15/2}$	356	360 [16]
02	$^4I_{15/2} \rightarrow ^4G_{9/2}$	364	364.9 [15]
03	$^4I_{15/2} \rightarrow ^4G_{11/2}$	378	378.79 [16]
04	$^4I_{15/2} \rightarrow ^2G_{9/2}$	406	406.5 [16]
05	$^4I_{15/2} \rightarrow ^4F_{3/2}$	441	442.5 [15]
06	$^4I_{15/2} \rightarrow ^4F_{5/2}$	450	450.45 [16]
07	$^4I_{15/2} \rightarrow ^4F_{7/2}$	486	487.81 [16]
08	$^4I_{15/2} \rightarrow ^2H_{11/2}$	520	520.83 [16]
09	$^4I_{15/2} \rightarrow ^4S_{3/2}$	542	545.6 [15]
10	$^4I_{15/2} \rightarrow ^4F_{9/2}$	650	651.5 [16]
11	$^4I_{15/2} \rightarrow ^4I_{9/2}$	800	800.03 [16]
12	$^4I_{15/2} \rightarrow ^4I_{11/2}$	970	975.61 [14]
13	$^4I_{15/2} \rightarrow ^4I_{13/2}$	1530	1526.02 [14]

Apart from these latter peaks, which remain stable after heat-treatments, spectacular changes in the shape of the absorption spectra can be observed for both annealing temperatures. This colour change results from copper and sodium reduction. The yellow-green coloration can be attributed to the formation of sodium NPs, while the red-brown coloration is more related to copper NPs, as reported in the literature [17, 18]. The amount of reduced sodium should be rather small, as should the corresponding amount of oxygen or fluorine. Chemical reduction may arise from Cu^+ or from reducing impurities that are common in fluoride glass batches. The following observations support the hypothesis of NPs formation:

- As shown in Table 1, changes in transparency and colour are observed according to the temperature and duration of the annealing process.

- We note the appearance of an absorption band at 410 nm; as reported by E. Kolobkova and N. Nikonorov [17]; sodium NPs are evidenced by their own absorption band in the 400-450 nm region, which is induced by the surface plasmon resonance.

- There is high absorption at wavelengths lower than 590 nm, particularly for the samples annealed at 270°C for 6h and 8h, (Fig. 5). In particular, the absorption peak near 560 – 570 nm is likely to correspond to the plasmon resonance of copper NPs [18-23].

- The absorption coefficient of the NZCE10 sample is almost constant at wavelengths ranging from 300 to 590 nm. This could be explained by the saturation of the absorption due to the strong presence of copper NPs. This is not the case for the NZCE11 sample heat-treated for 8h at 270°C. The image of this glass, shown in Table 1, evinces a mix of yellow-green and red-brown colorations. This observation can be explained by the decomposition of copper NPs, leading to a decrease in copper NPs concentration and a subsequent decrease in the absorption coefficient. For this reason, no absorption saturation was observed for the NZCE11sample.

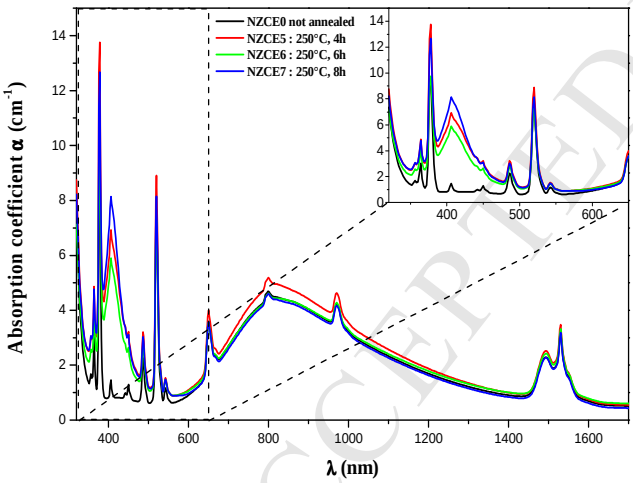

Fig. 4: Variation in absorption depending on annealing time at 250°C.

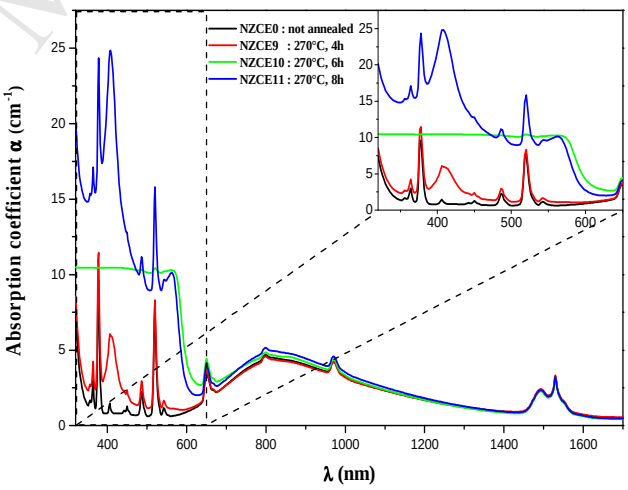

Fig. 5: Variation in absorption depending on annealing time at 270°C.

3.3. IR transmission (FTIR)

Fig. 6 shows the FTIR spectra of undoped 60mol%$NaPO_3$-40mol%ZnF_2 glass (NZ) and doped glass (NZCE).The FTIR spectra allowed us to determine the IR absorption edge of the studied glasses. It was estimated to be of the order of 4.2 µm, corresponding to the first overtone of the P-O vibration,

as already reported for fluorophosphate glasses [6]. A wide absorption band due to OH was observed around 3300 nm.

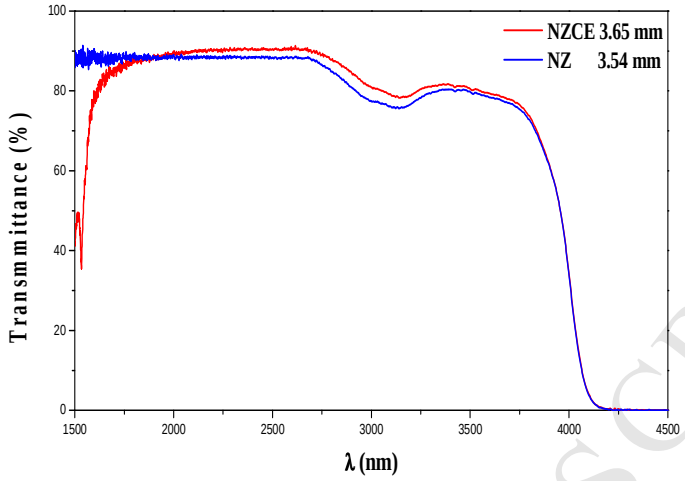

Fig. 6**:** FTIR spectra of NZ and NZCE glasses

3.4. SEM and TEM analyses

ASEM image of the cross-section of a cut edge of NZCE10glass is shown in Fig.7. Submicronic nanoparticles can clearly be seen inside the glass sample. They consist of relatively well-dispersed 0.5 µm-sized particles surrounded by smaller NPs with diameters of less than 100 nm.

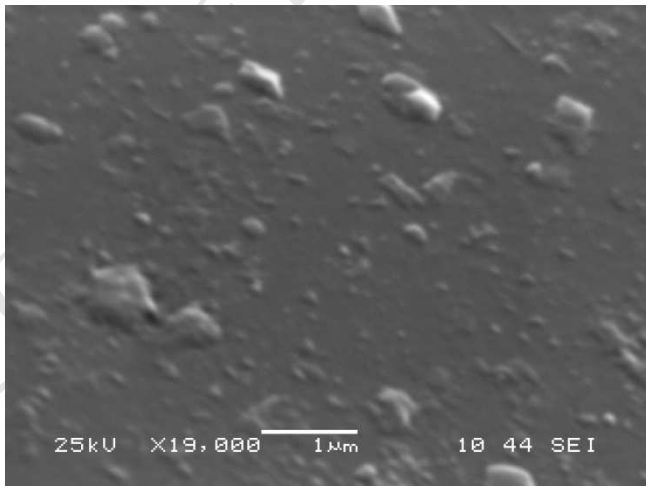

Fig. 7**:** SEM image of a cross-section of the NZCE10 glass

The elements present in the glass sample were identified using the energy-dispersive spectroscopic (EDS) technique with the TEM microscope. Fig.8 shows the EDS spectrum of NZCE10, which confirms the presence of the starting elements. Note that the presence of Ni and C is related to the

grid substrate used for TEM measurements. Combined with the above XRD patterns, the samples are further proven to be NZCE in their composition.

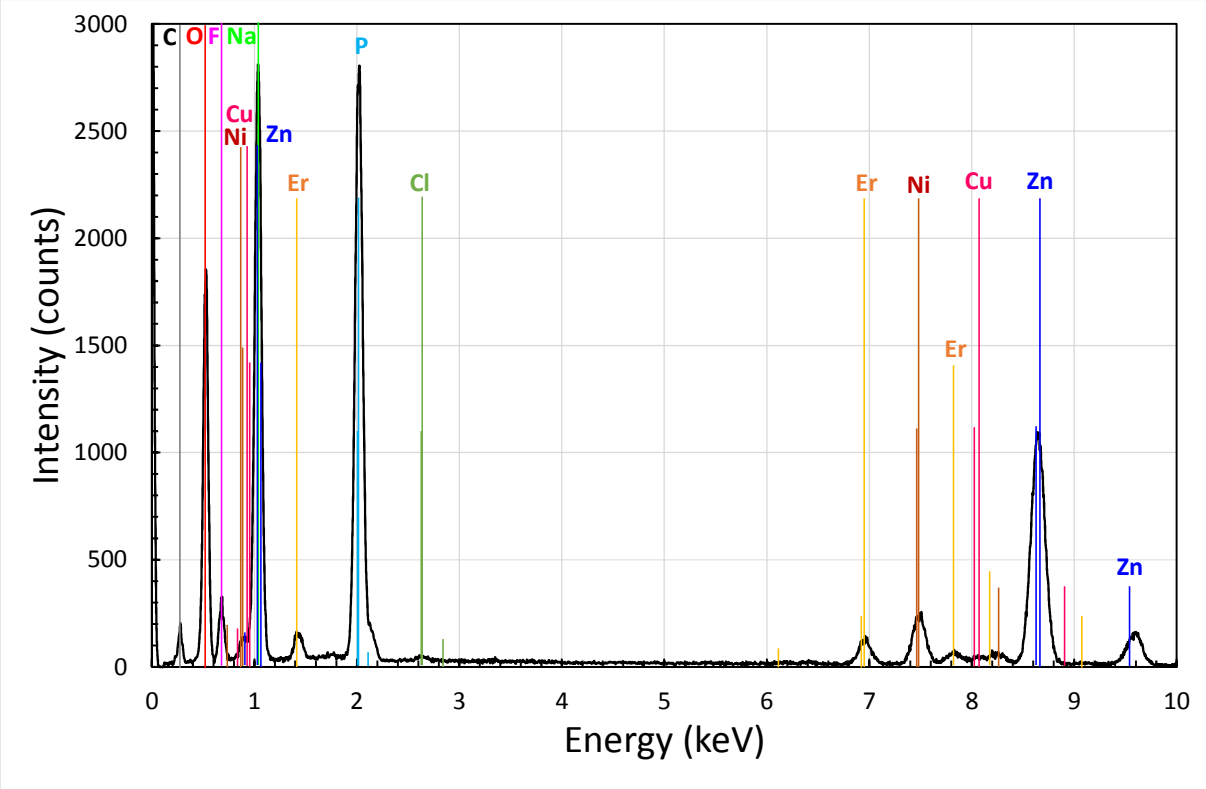

Fig.8: EDS spectrum of the NZCE10 glass

TEM observation showed relatively well-dispersed grains of about 5 μm in diameter. One representative particle was selected and analysed in agreement with the above EDS spectrum.

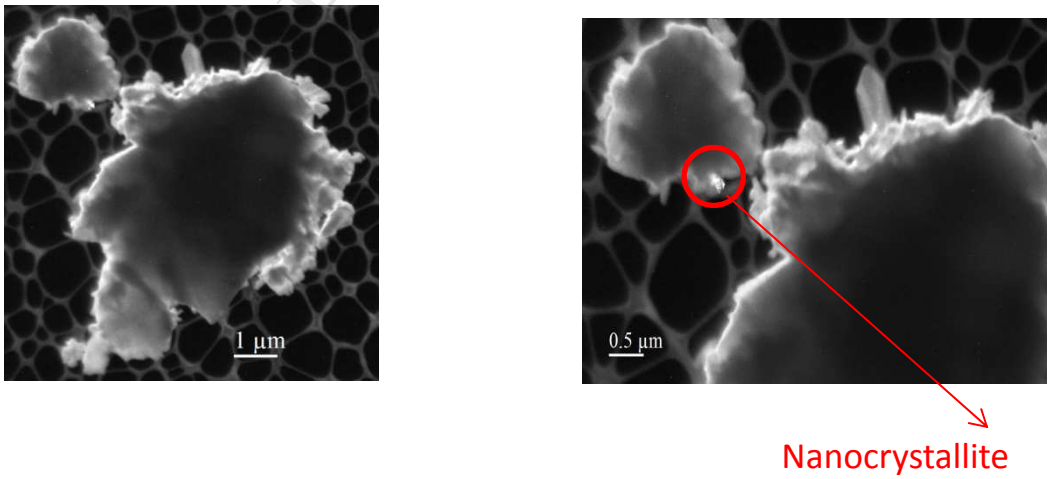

Fig.9: Dark field TEM image of a powder grain of NZCE10 glass

The grain image (Fig. 9), taken in dark field mode, shows the presence of a nanocrystallite, which could not be completely analysed and identified since the grain was subjected to strong mechanical and thermal variations under electron beam radiation.

3.5. Judd-Ofelt analysis

In this section, the intensity parameters Ω_t (t = 2, 4, 6) and spontaneous emission probabilities of Er^{3+} ions in the glass are determined by application of the Judd-Ofelt theory [24, 25] to the oscillator strengths deduced from absorption spectra. The calculation procedure has been widely described in the literature. The most essential formulae are recalled below. The experimental dipole line strength of a transition between two states of a single ion is related to the absorption spectrum through the relation:

$$S_m = 4\pi\varepsilon_0 \frac{3hc(2j+1)}{8\pi^3 e^2 \lambda_0} n \left(\frac{3}{n^2+2}\right)^2 \int \sigma(\lambda) d\lambda \quad (2)$$

where ε_0 is the vacuum permittivity, h is the Planck constant, c is the velocity of light and e is the electron charge. λ_0, j and n are respectively the centered wavelength of the specified transition, the total angular momentum of the ground state and the refractive index corresponding to λ_0. $\sigma(\lambda)$ is the absorption cross section given by:

$$\sigma(\lambda) = \frac{2.303 Do(\lambda)}{Nd} \quad (3)$$

where Do is the optical density ($Do(\lambda) = -log\left(\frac{I_0(\lambda)}{I(\lambda)}\right)$), N is the Er^{3+} ion concentration and d is the sample thickness.

The theory developed by Judd [24] and simultaneously by Ofelt [25] has been established for forced electric dipole transitions within the $4f$ configuration.The theoretical electric dipole line strengths of such transitions between two states $|SLJ\rangle$ and $|S' L' J'\rangle$ are expressed as a function of the intensity parameters Ω_t and the doubly-reduced unit tensor operators $\left|\langle SLJ||U^{(t)}||S' L' J'\rangle\right|^2$, calculated as follows:

$$S_{ed} = \sum_{t=2,4,6} \Omega_t \left|\langle SLJ||U^{(t)}||S' L' J'\rangle\right|^2 \quad (4)$$

The oscillator strengths are related to the dipole line strengths through the relations:

$$f_m = 4\pi\varepsilon_0 \frac{mc^2}{\pi e^2 \lambda_0^2} \int \sigma(\lambda) d\lambda \quad (5)$$

$$f_{calc} = \frac{8\pi^2 mc}{3h\lambda_0(2j+1)n^2} \left[n \left(\frac{n^2+2}{3}\right)^2 S_{ed} + n^3 S_{md} \right] \quad (6)$$

The three intensity parameters (Ω_t) include radial integrals, odd terms of the crystal field and perturbation energy denominators. These parameters maybe regarded as phenomenological, characterizing the radiative transition probabilities within the $4f^n$ configuration in a specific environment. They enable us to calculate emission probabilities and to predict other important radiative properties for the materials, such as radiative lifetimes and branching ratios. These parameters are usually determined from a least-square fit to the values of the experimental oscillator strengths using Eq. (4).

The quality of the fit is expressed by the magnitude of the root-mean-square deviation (RMS), defined by:

$$RMS = \sqrt{\frac{\sum(f_{calc} - f_m)^2}{p-3}} \tag{7}$$

where p is the number of observed transitions of the absorption spectrum, 3 stands for the number of adjusted parameters in the fit, and f_{calc} and f_m are respectively predicted and experimental oscillator strengths.

The total spontaneous emission probability from the excited state J' to the ground state J, including the contribution from electric and magnetic dipole transitions, is given by:

$$A_{JJ'} = \frac{64\pi^3}{3h(2J+1)\lambda_0^3}\frac{e^2}{4\pi\varepsilon_0}\left[n\left(\frac{n^2+2}{3}\right)^2 S_{ed} + n^3 S_{md}\right] \tag{8}$$

where S_{md} is the magnetic dipole line strength defined by:

$$S_{md} = \left(\frac{\hbar}{2m_e c}\right)^2 |\langle SLJ||(L+2S)||S'L'J'\rangle|^2 \tag{9}$$

The radiative lifetime τ_R of the excited state J' is simply related to the total spontaneous emission probability $A_{JJ'}$ by:

$$\tau_R = \frac{1}{A_{JJ'}} \qquad with \quad A_{JJ'} = \sum_{J''} A_{J'J''} \tag{10}$$

J''being the intermediate states lying between $J'$and J.

The branching ratio $\beta_{J'J''}$ corresponding to the emission from the excited level J' to level J'' intermediate between J' and the ground state J is easily estimated by:

$$\beta_{J'J''} = \frac{A_{J'J''}}{A_{JJ'}} = \tau_R A_{J'J''} \tag{11}$$

Among the transitions observed in the absorption spectrum from the $^4I_{15/2}$ (Er^{3+}) ground state to other states of the $4f^{11}$ (Er^{3+}) configuration, taking into account the selection rules, only the $^4I_{15/2} \rightarrow {}^4I_{13/2}$ and the $^4I_{15/2} \rightarrow {}^2K_{15/2}$ transitions exhibited a magnetic dipole character. The intensity parameters Ω_t were then adjusted by a least squares procedure, minimizing the sum of

squares of the deviations between the measured and theoretical dipole line strengths [24, 25]. The experimental dipole line strengths are compared with calculated ones in Table 4.

Table 4. Experimental and predicted oscillator strengths of Er^{3+} optical transitions in NZCE glass (2 mol% ErF_3); $\boldsymbol{\lambda_0}$ is the mean wavelength of the transition in nm; $\boldsymbol{n}$ is the refractive index.

Transition	$\boldsymbol{\lambda_0}$ $(\boldsymbol{nm})$	$\boldsymbol{n}$	$\boldsymbol{f_m}$ $(\boldsymbol{10^{-6}})$	$\boldsymbol{f_{calc}}(\boldsymbol{10^{-6}})$
$^4I_{15/2} \rightarrow {}^2K_{15/2}$	356	1.537	0.17(ed+md)	0.54(ed+md)
$^4I_{15/2} \rightarrow {}^4G_{9/2}$	364	1.535	1.58	1.49
$^4I_{15/2} \rightarrow {}^4G_{11/2}$	378	1.531	12.48	12.53
$^4I_{15/2} \rightarrow {}^2G_{9/2}$	406	1.525	0.68	0.64
$^4I_{15/2} \rightarrow {}^4F_{3/2}$	442	1.519	0.08	0.29
$^4I_{15/2} \rightarrow {}^4F_{5/2}$	450	1.518	0.34	0.49
$^4I_{15/2} \rightarrow {}^4F_{7/2}$	486	1.513	1.86	1.80
$^4I_{15/2} \rightarrow {}^2H_{11/2}$	520	1.510	7.02	6.98
$^4I_{15/2} \rightarrow {}^4S_{3/2}$	542	1.508	0.41	0.40
$^4I_{15/2} \rightarrow {}^4F_{9/2}$	650	1.502	2.03	2.10
$^4I_{15/2} \rightarrow {}^4I_{9/2}$	800	1.498	0.45	0.38
$^4I_{15/2} \rightarrow {}^4I_{11/2}$	970	1.495	0.56	0.51
$^4I_{15/2} \rightarrow {}^4I_{13/2}$	1530	1.491	1.82(ed+md)	1.56(ed+md)

The set of calculated intensity parameters for Er^{3+} in NZCE glass is:

$\boldsymbol{\Omega_2} = (4.35 \pm 0.08) \times 10^{-20} cm^2$

$\boldsymbol{\Omega_4} = (1.87 \pm 0.12) \times 10^{-20} cm^2$

$\boldsymbol{\Omega_6} = (1.08 \pm 0.08) \times 10^{-20} cm^2$

The accuracy of the fit given by the RMS deviation, calculated as 0.11×10^{-6} here, is consistent with that generally obtained for glasses.

The calculated intensity parameters for Er^{3+} in NZCE glass are shown in Table 5 with those obtained for some other host materials for comparison. These parameters depend on the host glass composition. As established by Jørgensen and Reisfeld [26], the Ω_2 parameter is mainly determined by the covalent character of the chemical bonding, while Ω_4 and Ω_6 are related to the rigidity of the host. From Table 5, $\Omega_{2,4,6}$ are the highest for the studied glass, except for the Ω_6 parameter, which is larger in NPP glass [27].

Table 5. Intensity parameters of some hosts for comparison.

Glass	Composition (mol%)				Ω ($10^{-20}cm^2$)			Refs.
					Ω_2	Ω_4	Ω_6	
NZCE	$60NaPO_3$	$37.5ZnF_2$	$0.5CuCl$	$2ErF_3$	4.35	1.87	1.08	This work
NPP	$30Na_2O$	$30PbCl_2$	$40P_2O_5$	$1ErCl_3$	3.79	0.13	1.21	[27]
NCE	$75NaPO_3$	$24CaF_2$	$1\ ErF_3$		2.25	1.01	0.80	[28]
NBE	$75NaPO_3$	$24BaF_2$	$1\ ErF_3$		2.27	0.86	0.84	[29]
SBNE	$59.5SiO_2$	$20B_2O_3$	$20Na_2O$	$0.5Er_2O_3$	3.87	1.54	0.72	[30]

The spontaneous emission probabilities, radiative lifetime and branching ratio calculated for the different transitions of Er^{3+} in the NZCE glass are summarized in Table 6.

Table 6. Predicted dipole line strengths $\boldsymbol{S_{ed}}$ and $\boldsymbol{S_{md}}$, radiative spontaneous emission probabilities $\boldsymbol{A_{ed}}$ and $\boldsymbol{A_{md}}$, branching ratio $\boldsymbol{\beta}$, and radiative lifetimes $\boldsymbol{\tau_{rad}}$ of the Er^{3+} transition from excited states to ground state in NZCE0 glass.

Transition	$\boldsymbol{S_{ed}}$	$\boldsymbol{S_{md}}$	$\boldsymbol{A_{ed}}$	$\boldsymbol{A_{md}}$	$\boldsymbol{\beta}$	$\boldsymbol{\tau_{rad}}$
	$10^{-20}cm^2$		s^{-1}			ms
$^2K_{15/2} \rightarrow\ ^2H_{11/2}$	1.67	0.00	155.47	0.00	0.10	
$^2K_{15/2} \rightarrow\ ^4F_{9/2}$	0.16	0.00	43.98	0.00	0.03	
$^2K_{15/2} \rightarrow\ ^4I_{9/2}$	0.52	0.00	271.31	0.00	0.17	
$^2K_{15/2} \rightarrow\ ^4I_{11/2}$	0.48	0.00	369.70	0.00	0.23	
$^2K_{15/2} \rightarrow\ ^4I_{13/2}$	0.03	0.01	45.01	15.10	0.04	
$^2K_{15/2} \rightarrow\ ^4I_{15/2}$	0.19	0.02	604.09	72.13	0.43	0.630
$^4G_{9/2} \rightarrow\ ^4F_{7/2}$	2.79	0.00	195.61	0.02	0.01	
$^4G_{9/2} \rightarrow\ ^2H_{11/2}$	0.87	0.33	104.12	43.81	0.01	
$^4G_{9/2} \rightarrow\ ^4F_{9/2}$	1.95	0.01	744.44	6.29	0.05	
$^4G_{9/2} \rightarrow\ ^4I_{11/2}$	0.69	0.00	767.56	1.02	0.05	
$^4G_{9/2} \rightarrow\ ^4I_{13/2}$	5.42	0.00	11158.02	0.00	0.70	
$^4G_{9/2} \rightarrow\ ^4I_{15/2}$	0.58	0.00	2834.74	0.00	0.18	0.063
$^4G_{11/2} \rightarrow\ ^4F_{9/2}$	1.93	0.01	471.21	2.57	0.02	
$^4G_{11/2} \rightarrow\ ^4I_{9/2}$	0.36	0.00	178.15	0.75	0.01	
$^4G_{11/2} \rightarrow\ ^4I_{13/2}$	1.22	0.02	1787.53	39.99	0.09	
$^4G_{11/2} \rightarrow\ ^4I_{15/2}$	5.10	0.00	18288.92	0.00	0.87	0.048
$^2G_{9/2} \rightarrow\ ^2H_{11/2}$	0.55	0.02	18.40	0.84	0.01	

Table 6. Predicted dipole line strengths S_{ed} and S_{md}, radiative spontaneous emission probabilities A_{ed} and A_{md}, branching ratio β, and radiative lifetimes τ_{rad} of the Er^{3+} transition from excited states to ground state in NZCE0 glass.

Transition	S_{ed}	S_{md}	A_{ed}	A_{md}	β	τ_{rad}
	$10^{-20}cm^2$		s^{-1}			ms
$^2G_{9/2} \rightarrow {}^4F_{9/2}$	0.12	0.19	20.75	37.04	0.02	
$^2G_{9/2} \rightarrow {}^4I_{9/2}$	0.08	0.00	30.99	0.47	0.01	
$^2G_{9/2} \rightarrow {}^4I_{11/2}$	0.46	0.04	295.82	31.13	0.12	
$^2G_{9/2} \rightarrow {}^4I_{13/2}$	0.94	0.00	1238.59	0.00	0.47	
$^2G_{9/2} \rightarrow {}^4I_{15/2}$	0.28	0.00	959.02	0.00	0.36	0.378
$^4F_{3/2} \rightarrow {}^4F_{9/2}$	0.07	0.00	14.61	0.00	0.01	
$^4F_{3/2} \rightarrow {}^4I_{9/2}$	0.49	0.00	273.29	0.00	0.14	
$^4F_{3/2} \rightarrow {}^4I_{11/2}$	0.70	0.00	707.16	0.00	0.35	
$^4F_{3/2} \rightarrow {}^4I_{13/2}$	0.04	0.00	85.39	0.00	0.04	
$^4F_{3/2} \rightarrow {}^4I_{15/2}$	0.14	0.00	903.60	0.00	0.45	0.501
$^4F_{5/2} \rightarrow {}^4F_{9/2}$	0.84	0.00	95.64	0.00	0.04	
$^4F_{5/2} \rightarrow {}^4I_{9/2}$	0.26	0.00	87.20	0.00	0.04	
$^4F_{5/2} \rightarrow {}^4I_{11/2}$	0.19	0.00	113.10	0.00	0.05	
$^4F_{5/2} \rightarrow {}^4I_{13/2}$	0.70	0.00	992.30	0.00	0.43	
$^4F_{5/2} \rightarrow {}^4I_{15/2}$	0.24	0.00	999.32	0.00	0.44	0.436
$^4F_{7/2} \rightarrow {}^4I_{9/2}$	0.71	0.07	100.48	11.07	0.04	
$^4F_{7/2} \rightarrow {}^4I_{11/2}$	0.67	0.00	196.19	0.00	0.06	
$^4F_{7/2} \rightarrow {}^4I_{13/2}$	0.63	0.00	473.87	0.00	0.15	
$^4F_{7/2} \rightarrow {}^4I_{15/2}$	0.95	0.00	2323.24	0.00	0.74	0.320
$^2H_{11/2} \rightarrow {}^4I_{9/2}$	1.34	0.01	72.60	0.58	0.01	
$^2H_{11/2} \rightarrow {}^4I_{11/2}$	0.45	0.05	57.60	7.25	0.01	
$^2H_{11/2} \rightarrow {}^4I_{13/2}$	0.27	0.14	100.31	58.64	0.03	
$^2H_{11/2} \rightarrow {}^4I_{15/2}$	3.97	0.00	5232.59	0.00	0.94	0.180
$^4S_{3/2} \rightarrow {}^4I_{9/2}$	0.42	0.00	47.52	0.00	0.04	
$^4S_{3/2} \rightarrow {}^4I_{11/2}$	0.09	0.00	25.42	0.00	0.02	
$^4S_{3/2} \rightarrow {}^4I_{13/2}$	0.38	0.00	343.04	0.00	0.27	
$^4S_{3/2} \rightarrow {}^4I_{15/2}$	0.24	0.00	833.51	0.00	0.67	0.800

Table 6. Predicted dipole line strengths S_{ed} and S_{md}, radiative spontaneous emission probabilities A_{ed} and A_{md}, branching ratio β, and radiative lifetimes τ_{rad} of the Er^{3+} transition from excited states to ground state in NZCE0 glass.

Transition	S_{ed}	S_{md}	A_{ed}	A_{md}	β	τ_{rad}
	$10^{-20}cm^2$		s^{-1}			ms
$^4F_{9/2} \rightarrow {}^4I_{11/2}$	1.72	0.19	47.91	5.84	0.04	
$^4F_{9/2} \rightarrow {}^4I_{13/2}$	0.41	0.00	60.57	0.00	0.05	
$^4F_{9/2} \rightarrow {}^4I_{15/2}$	1.50	0.00	1194.22	0.00	0.91	0.761
$^4I_{9/2} \rightarrow {}^4I_{11/2}$	0.28	0.39	0.62	0.98	0.01	
$^4I_{9/2} \rightarrow {}^4I_{13/2}$	0.80	0.00	36.13	0.00	0.20	
$^4I_{9/2} \rightarrow {}^4I_{15/2}$	0.33	0.00	141.32	0.00	0.79	5.585
$^4I_{11/2} \rightarrow {}^4I_{13/2}$	1.64	0.78	15.64	8.31	0.18	
$^4I_{11/2} \rightarrow {}^4I_{15/2}$	0.55	0.00	108.44	0.00	0.82	7.553
$^4I_{13/2} \rightarrow {}^4I_{15/2}$	1.85	0.71	79.06	33.74	1.00	8.865

4. Simulation of the spectroscopic behaviour of copper nanoparticles

The spectroscopic behaviour of a copper nanosphere in a vitreous environment having the same refractive index as our samples was studied using the finite element method. The simulation scheme is illustrated in the Fig.10.

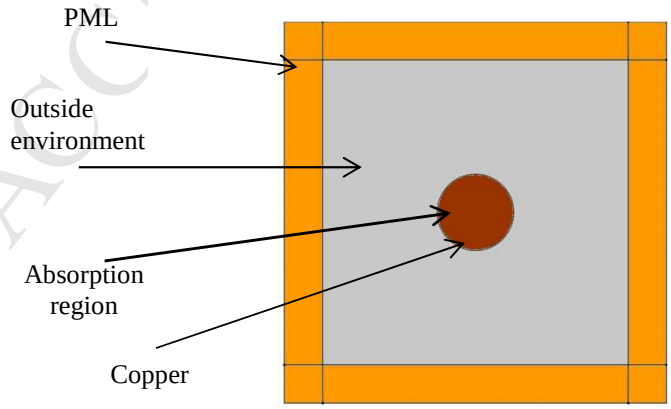

Fig. 10: Simulation scheme of a copper nanosphere in a vitreous environment

The absorption cross section $\boldsymbol{\sigma_{abs}}$ can be defined by:

$$\sigma_{abs} = \frac{W_{abs}}{P_{inc}} \tag{12}$$

where W_{abs} and P_{inc} are respectively the rate of energy absorbed by the particle and the incident irradiation defined as the energy flux of the incident wave, given by the time average of the Poynting vector:

$$P = \frac{1}{2} Re[E \times H^*] \tag{13}$$

The energy absorbed by the particle is then expressed by:

$$W_{abs} = \iiint_{V_p} Q_{loss} dV \tag{14}$$

where V_p is the volume of the particle and Q_{loss} is the rate of energy loss in the particle

$$Q_{loss} = \frac{1}{2} Re[J_{tot} \cdot E^* + j\omega B \cdot H^*] \tag{15}$$

where the total J_{tot} current is the superposition of conduction and displacement currents:

$$J_{tot} = \sigma E + j\omega D \tag{16}$$

Finally, the rate of energy absorbed by the particle is written:

$$W_{abs} = \frac{1}{2} \iiint_{V_p} Re[(\sigma E + j\omega D) \cdot E^* + j\omega B \cdot H^*] \tag{17}$$

Absorption spectra for copper nanospheres of different sizes were calculated; the results are shown in Fig.11.

A strong absorption around 590 nm is observed, similar to that observed experimentally for NZCE10 and NZCE11 (Fig.5).

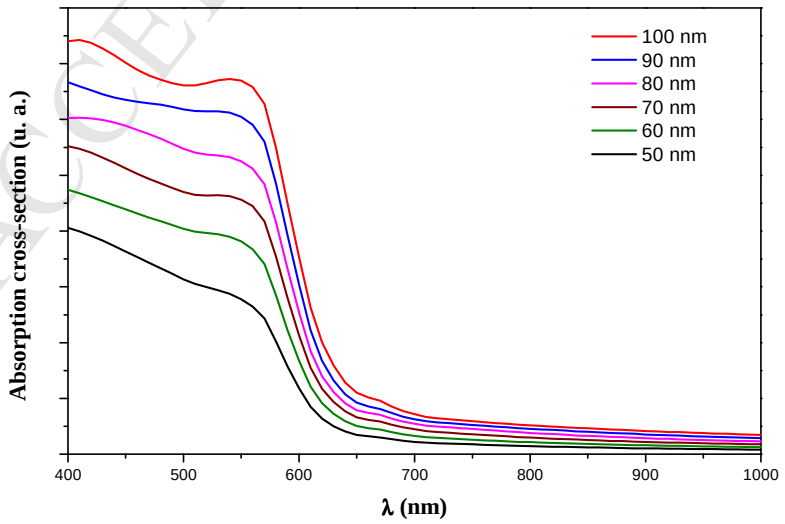

Fig.11: Theoretical absorption spectra of copper nanoparticles of different sizes

5. Conclusions

Fluorophosphate glasses co-doped with rare earth and transition metal were synthesized and characterized. These glasses are transparent, with a blue colour which turns to red when the annealing temperature increases. Thermal analysis shows that this vitreous matrix presents a good thermal stability with respect to devitrification. The refractive index is close to 1.5 with limited variation versus wavelength beyond 600 nm. Observation of the UV-Visible and NIR absorption spectra emphasizes the typical absorption bands corresponding to Er^{3+} ions. The appearance of a supplementary absorption band at 410 nm upon heat-treatment is consistent with the formation of sodium NPs. The red coloration was attributed to copper NPs, which magnify absorption for wavelengths lower than 590 nm through surface plasmon resonance. The intensity parameters ($\Omega_{2,4,6}$) of the NZCE0 glass were calculated based on the experimental absorption spectrum and Judd–Ofelt theory. They were then used to determine radiative spectroscopic properties such as the spontaneous emission probabilities A_{ij} (s^{-1}), branching ratio β and radiative lifetimes (τ_{rad}) of the Er^{3+} transition from excited states to ground state in this glass.

Acknowledgements

This research was performed as a part of joint PHC-Tassili, Algeria-France R&D Project (project N° 16MDU959) supported by Campus France (project N° 35079VB).

N.A is grateful to the MESRS from Algeria for providing a grant under the PNE program 2016-2017. It's also grateful for the ICCF-UMR 6296 and the ICR-UMR 6226 for granting access to their facilities and for their visiting scientist support.

References

[1] K. Kiran Kumar, P. Manasa, N. Vijaya, J. Kaewkhao and C.K. Jayasankar, Spectroscopic investigation and optical properties of Eu^{3+}-doped fluorophosphates glasses, Key. Eng. Mater. ISSN: 1662-9795, vols. 675-676 (2016) 418-423.

[2] K. Linganna, K. Suresh, S. Ju, W.-T. Han, C.K. Jayasankar, and V. Venkatramu, Optical properties of Er^{3+}-doped K-Ca-Al fluorophosphates glasses for optical amplification at 1.53 μm, Opt. Mater. Express 5 (8) (2015) 1689.

[3] B. Karmakar, P. Kundu, and R. N. Dawivedi, Infrared spectroscopic method for determination of thermal properties of fluorophosphates glasses, J. Am. Ceram. Soc. 83(5) (2000) 1305-1307.

[4] R. K. Sandwick, R. Scheller, and K. H. Mader, Production of high homogeneous fluorophosphates laser glass, Los Angeles Technical Symposium, International Society for Optics and Photonics 171 (1979) 161–164.

[5] M. Matecki, and M. Poulain, Transition metal fluorophosphate glasses, J. Non-Cryst. Solids 56(1) (1983) 111-116.

[6] T. Djouama, A. Boutarfaia and M. Poulain, Fluorophosphate glasses containing manganese, J. Phys. Chem. Solids 69(11) (2008) 2756-2763.

[7] M. Matecki, N. Duhamel and J. Lucas, Sodium fluorophosphate glasses with high rare earth ion concentration, J. Non-Cryst. Solids 184 (1995) 273-277.

[8] M. Liao, Z. Chao Duan, L. Hu, Y. Fang and L. Wen, Spectroscopic properties of Er^{3+}/Yb^{3+}codoped fluorophosphate glasses, J. Lumin. 126 (2007) 139-144.

[9] A. Nommeots-Nomm, N.G. Boetti, T. Salminen, J. Massera, M. Hokka and L. Petit, Luminescence of Er^{3+} doped oxyfluoride phosphate glasses and glass-ceramics, J. Alloys Compd. 751 (2018) 224-230.

[10] S. A. Tijani, S. M. Kamal, Y. Al-hadeethi, M. Arib, M.A. Hussein, S. Wagehand and L.A. Dim, Radiation shielding properties of transparent erbium zinc tellurite glass system determined at medical diagnostic energies, J. Alloys Compd. 741 (2018) 293-239.

[11] M. R. Dousti, M. Sahar, S. K. Ghoshal, R. J. Amjad and R. Arifin, Up-conversion enhancement in Er^{3+}-Ag co-doped zinc tellurite glass: Effect of heat treatment, J. Non-Cryst. Solids 358(22) (2012) 2939-2942.

[12] L. P. N.Riano, C. B. de Araujo, O. L. Malta, P. Santa Cruz, and A. Couto dos Santos, Growth of metallic Ag nanoparticles in fluoroborate glasses doped with rare earth ions and their optical characterization, International Society for Optics and Photonics (2004).

[13] D. K. Sardar, J.B. Gruber, B. Zandi, J. A. Hutchinson and C. W. Trussell, Judd-Ofelt analysis of the $Er^{3+}(4f^{11})$ absorption intensities in phosphate glass: Er^{3+}, Yb^{3+}, J. Appl. Phys. 93(4) (2003) 2041-2046.

[14] Z. A. S. Mahraz, M. R. Sahar, S. K. Ghoshal and M. R. Dousti, Concentration dependent luminescence quenching of Er^{3+}-doped zinc boro-tellurite glass, J. Lumin. 144 (2013) 139-145.

[15] B. Karmakar, and R. N. Dwivedi, FT-IRRS, UV-Vis-NIR absorption and green upconversion in Er^{3+} doped lead silicate glass, J. Non-Cryst. Solids 342(1) (2004) 132-139.

[16] W. A. Pisarski, Spectroscopic analysis of praseodymium and erbium ions in heavy metal fluoride and oxide glasses, J. Mol. Struct. 744 (2005) 473-479.

[17] E. Kolobkova and N. Nikonorov, Metal sodium nanoparticles in fluorophosphate glasses, J. Alloys Compd. 637 (2015) 545-551.

[18] P. Colomban, Nanoparticules et couleur, une tradition millénaire, Photoniques (2015) 37-41.

[19] Y. Teng, B. Qian, N. Jiang, Y. Liu, F. Luo, S. Ye, J. Zhou, B. Zhu, H. Zeng and J. Qiu, Light and heat driven precipitation of copper nanoparticles inside Cu^{2+}-doped borate glasses, Chem. Phys. Lett. 485(1) (2010) 91-94.

[20] Z. W. Dong, X. C. Yang, Z. H. Li, J. X. Xu, K. J. Liu, C. F. Zhang, G. J. You, Y. L. Yan and S. X. Qian, Ultrafast dynamics of copper nanoparticles embedded in soda-lime silicate glass fabricated by ion exchange, Thin Solid Films 517(21) (2009) 6046-6049.

[21] P. Yaduvanshi, A. Mishra, S. Kumar and R. Dhar, Enhancement in the thermodynamic, electrical and optical properties of hexabutoxytriphenylene due to copper nanoparticles, J. Mol. Liq. 208 (2015) 160-164.

[22] S. Kubota, T. Morioka, M. Takesue, H. Hayashi, M. Watanabe and R. L. Smith Jr, Continuous supercritical hydrothermal synthesis of dispersible zero-valent copper nanoparticles for ink applications in printed electronics, J. Supercrit. Fluids 86 (2014) 33-40.

[23] M. Noguchi, H. Kazama, A. Katoh, Y. Uchida and K. Matsui, Photoinduced degradation of fluorescence and formation of copper nanoparticles in sol-gel silica doped with flavins, J. Non-Cryst. Solids 357(15) (2011) 2966-2969.

[24] B. R. Judd, Optical absorption intensities of rare-earth ions, Phys. Rev. 127 (1962) 750-761.

[25] G. S. Ofelt, Intensities of crystal spectra of rare earth ions, J. Chem. Phys. 37 (1962) 511-520.

[26] C. K. Jørgensen, and R. Reisfeld, Judd-Ofelt parameters and chemical bonding, J. Less-Com. Metals 93 (1983) 107-112.

[27] K. Pradeesh, C. J. Oton, V. K. Agotiya, M. Raghavendra and G. V. Prakash, Optical properties of Er^{3+} doped alkali chlorophosphate glasses for optical amplifiers, Opt. Mater. 31 (2008) 155-160.

[28] K. Bennemans, R. Van Deun, C. Görller-Walrand and J-L. Adam, Spectroscopic properties of trivalent lanthanide ions in fluorophosphate glasses, J. Non-Cryst. Solids 238 (1998) 11-29.

[29] R. Van Deun, K. Bennemans, C. Görller-Walrand and J-L. Adam, Judd-Ofelt intensity properties of trivalent lanthanide ions in a $NaPO_3$-BaF_2 based fluorophosphates glass, J. Alloys Compd. 283 (1999) 59-65.

[30] S. Liu, G. Zhao, Y. Li, H. Ying, J. Wang and G. Han, Optical absorption and emission properties of Er^{3+} doped mixed alkali borosilicate glasses, Opt. Mater. 30 (2008) 1393-1398.

Highlights

- Fluorophosphate glasses have been synthesized in the NaP3-ZnF2 system and have been doped with Er3+ and Cu+.

- Copper and sodium nanoparticles have been formed into this vitrious matrix using heat treatement.

- Spectroscopic properties have been investigated and discussed on the basis of the Judd-Ofelt theory.